

Biomedical Physics & Engineering Express



PAPER


The time-dependent diffusivity in the abdominal ganglion of *Aplysia californica*: experiments and simulations

RECEIVED
21 February 2019

REVISED
19 June 2019

ACCEPTED FOR PUBLICATION
5 July 2019

PUBLISHED
23 July 2019

Khieu-Van Nguyen², Denis Le Bihan², Luisa Ciobanu² and Jing-Rebecca Li¹ 

¹ INRIA Saclay-Equipe DEFI, CMAP, Ecole Polytechnique Route de Saclay, 91128, Palaiseau Cedex, France

² NeuroSpin, CEA Saclay Center 91191 Gif-sur-Yvette Cedex France

E-mail: jingrebecca.li@inria.fr

Keywords: diffusion MRI, aplysia, ADC, simulation

Abstract

The nerve cells of the *Aplysia* are much larger than mammalian neurons. Using the *Aplysia* ganglia to study the relationship between the cellular structure and the diffusion MRI signal can potentially shed light on this relationship for more complex organisms. We measured the dMRI signal of chemically-fixed abdominal ganglia of the *Aplysia* at several diffusion times. At the diffusion times measured and observed at low b-values, the dMRI signal is mono-exponential and can be accurately represented by the parameter ADC (Apparent Diffusion Coefficient). We performed numerical simulations of water diffusion for the large cell neurons in the abdominal ganglia after creating geometrical configurations by segmenting high resolution T₂-weighted (T₂w) images to obtain the cell outline and then incorporating a manually generated nucleus. The results of the numerical simulations validate the claim that water diffusion in the large cell neurons is in the short diffusion time regime at our experimental diffusion times. Then, using the analytical short time approximation (STA) formula for the ADC, we showed that in order to explain the experimentally observed behavior, it is necessary to consider the nucleus and the cytoplasm as two separate diffusion compartments. By using a two compartment STA model, we were able to illustrate the effect of the highly irregular shape of the cell nucleus on the ADC.

1. Introduction

Using diffusion-encoding MRI to get tissue micro-structure information in the mammalian brain has been the focus of much experimental and modeling work in recent years (Assaf *et al* 2008, Alexander *et al* 2010, Zhang *et al* 2011, 2012, Burcaw *et al* 2015, Palombo *et al* 2017, 2016, Ning *et al* 2017). Biological quantities of interest include axon diameter (Assaf *et al* 2008, Zhang *et al* 2011, Burcaw *et al* 2015) and orientation (Alexander *et al* 2010, Zhang *et al* 2012), neurite density (Alexander *et al* 2010, Zhang *et al* 2012), and more recently, fiber structure (Palombo *et al* 2017). Experimental protocols that are robust and specific in the identification of these biological quantities have been subject of much research. The experimental parameters that can be varied include the diffusion time and the magnitude and direction of the diffusion-encoding gradients. When the MRI signal is acquired at low gradient magnitudes, the signal contains only

information about the Apparent Diffusion Coefficient (ADC).

The incoherent motion of water molecules during the diffusion encoding time causes a signal attenuation from which the ADC can be calculated (Hahn 1950, Stejskal and Tanner 1965, Bihan *et al* 1986). For unrestricted diffusion, the root mean square displacement of molecules is given by $\bar{x} = \sqrt{2dD_0t}$ (Berg 1993, Zhong and Gore 1991) where $d = 1, 2, 3$, for one, two and three dimensions, D_0 is the intrinsic diffusion coefficient, and t is the diffusion time. In biological tissue, the diffusion is usually hindered or restricted (e.g. by cell membranes) and the mean square displacement is smaller than in the case of unrestricted diffusion. Intuitively, more hinderance or restriction will occur for more molecules as the diffusion time increases, so we expect that the experimentally determined ADC will decrease with increasing diffusion time (Stejskal and Tanner 1965, Tanner and Stejskal 1968, Grebenkov 2007, Özarslan *et al* 2006).

As a result, the extent of the ADC decrease can be potentially used to gather information about the tissue micro-structure; by acquiring several diffusion weighted images with different diffusion times and fitting the data to a model. For example in (Dietrich *et al* 2014, Weber *et al* 2009), the authors determined cell size and membrane distance based on diffusion MRI with multiple diffusion times. Numerous biophysical models have been proposed, usually subdividing the tissue into compartments described by spheres, ellipsoids, cylinders, and the extra-cellular space (Assaf *et al* 2008, Alexander *et al* 2010, Zhang *et al* 2011, Burcaw *et al* 2015, Fieremans *et al* 2011, Panagiotaki *et al* 2012, Jespersen *et al* 2007). However, it is difficult to connect the geometrical parameters contained in these models to the ground truth values due to the complexity of the brain tissue.

In the mammalian brain, the sizes of neurons and glial cells are on the order of micrometers (Fiala *et al* 2012), whereas the size of the imaging voxel is on the order of hundreds of micrometers. This makes it extra-ordinarily difficult to disentangle the validation of ADC models from the problem of figuring out the underlying tissue geometry that gave rise to the measured signal. One approach to completely separate the ADC model validation from geometrical uncertainty is the construction and imaging of special phantoms, examples of which include carrot slices (Dietrich *et al* 2014), spheres filled with a gel in each cell component (Lavdas *et al* 2013), physical phantoms constructed from resected rat spinal cord (Campbell *et al* 2005), polyfil fibers wound on a spherical polyamide spindle (Moussavi-Biugui *et al* 2011), and straight X-crossings of polyester fibers (Pullens *et al* 2010). In the phantoms, the geometry can be said to be known more or less exactly. However, there is a big gap between the tissue cellular environment and the phantoms. In particular, cells have a nucleus, organelles, and the cells and cell components have a range of sizes and shapes. These effects are certainly present in the imaging of biological tissue and make the direct application of phantom studies results to brain imaging potentially immature.

The precedent considerations motivate our present work of imaging a neural network with much larger components (compared to mammalian cells) for which the geometrical information is easier to ascertain than for the mammalian brain tissue. The advantage of *Aplysia*'s nervous system is that the cellular structure is relatively simple, with some of the largest cells identifiable in the T_2w images we acquire along with the diffusion weighted images. We consider our work an intermediary between the imaging of the mammalian brain tissue and the imaging of specially constructed phantoms. In this sense, we use the *Aplysia* neural network as a 'biological phantom' for dMRI.

Because the *Aplysia* cells are much larger than the mammalian neural cells, for a given diffusion-encoding sequence, the relevant diffusion time regime

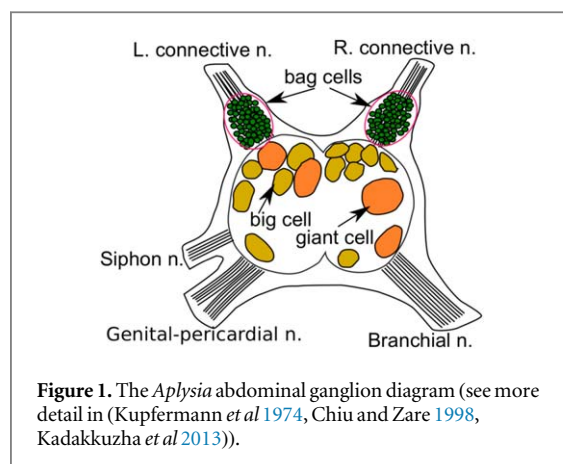


Figure 1. The *Aplysia* abdominal ganglion diagram (see more detail in (Kupfermann *et al* 1974, Chiu and Zare 1998, Kadakkuzha *et al* 2013)).

is longer for the *Aplysia* than for mammalian neurons. As a result, it is possible to work with the short diffusion time approximation while using the standard Pulsed Gradient Spin Echo (PGSE) (Stejskal and Tanner 1965) sequence, instead of resorting to more specialized sequences such as Oscillating Gradient (OGSE) (Does *et al* 2003) sequences.

2. Materials and methods

2.1. Animal model

The neural system of the *Aplysia californica* consists of five pairs of ganglia: buccal, cerebral, pleural, pedal, and abdominal (Kandel and Kupfermann 1970). The abdominal ganglion was chosen in this imaging study because the cellular network is very well known in terms of position and morphology of single cell neurons and axonal orientation (Conn and Kaczmarek 1989, Musio and Bedini 1990). Moreover, the abdominal ganglion or single neurons from the abdominal ganglion have been investigated using magnetic resonance microscopy (MRM) and diffusion MRM studies (Schoeniger *et al* 1994, Hsu *et al* 1997, Grant *et al* 2001, Lee *et al* 2015). The abdominal ganglion diagram is shown in figure 1.

In this imaging study, we focused on the large neuron cells. There are many large neuron cells in the abdominal ganglion with radii of at least $75 \mu\text{m}$ that are visible by inspection in the high resolution ($26 \mu\text{m}$ isotropic) T_2w images. Some of these include neurons L2 to L9, L11, R2 to R8, R14 and R15 (labeled L or R for left or right hemiganglion, e.g. see in (Kupfermann *et al* 1974)). The single cell neurons with radii smaller than $75 \mu\text{m}$ are not included in this group. We note that the sizes of these identified neurons are not fixed, they vary as a function of the age and the weight of the animal. The large cell neurons contain a nucleus, cytoplasm and are probably surrounded by small satellite (glial) cells (Lee *et al* 2015). The satellite cells are very small cells, $3 \mu\text{m}$ maximum in radius, without a nucleus (Conn and Kaczmarek 1989, Musio and Bedini 1990, Lee *et al* 2015).

Several large cell neurons of radii greater than $75 \mu\text{m}$ (up to $210 \mu\text{m}$) that are easily identifiable in the $T_2\text{w}$ image were selected for this study.

2.2. Sample preparation

Six *Aplysia californica* (National Resource for Aplysia, Miami, FL, USA) were used in this study. The animals were anesthetized by injection of an isotonic magnesium chloride solution (MgCl_2 , 360 mM; HEPES, 10 mM; pH = 7.5). All chemicals were purchased from Sigma-Aldrich (Lyon, France). The abdominal ganglion was resected and fixed with PFA 4% by immersion for 10 minutes and then washed three times in PBS pH = 7.4. For imaging, the abdominal ganglion was inserted into a 2.0 mm inner diameter (ID) glass capillary filled with fluorinert and then slid inside the transceiver coil.

2.3. Image acquisition

All experiments were performed at room temperature ($\approx 19^\circ\text{C}$) on a 17.2 T system (Bruker BioSpin, Ettlingen, Germany) equipped with 1.0 T m^{-1} gradients. Radio-frequency transceivers were home-built micro-coils with inner diameters of 2.4 mm, the design of which has been described in (Jelescu *et al* 2013, Radecki *et al* 2014). Typically, a $T_2\text{w}$ image and five to seven diffusion weighted images were acquired for each sample. The T_2 weighted image was acquired using a Rapid Acquisition with Refocused Echoes (RARE) with the following parameters: TR = 1500 ms, $\text{TE}_{\text{eff}} = 48$ ms, acceleration factor $A_F = 8$, isotropic spatial resolution $26 \mu\text{m}$, matrix size of $400 \times 88 \times 88$, 8 averages for an acquisition time of 3 hours 14 minutes. The acquisition parameters for the diffusion-weighted images (DP-FISP pulse sequence with bipolar diffusion gradients (Lu *et al* 2012)) were $\text{TE}/\text{TR} = 1.63/1000$ ms, 2 averages, isotropic spatial resolution $52 \mu\text{m}$, 3 directions (\vec{x} , \vec{y} , \vec{z}), four samples acquired with seven diffusion encoding times ($\delta = 2.5$ ms, $\Delta = [5, 7.5, 10, 12, 15, 20, 25]$ ms), one sample acquired with six diffusion encoding times ($\delta = 2.5$ ms, $\Delta = [5, 10, 12, 15, 20, 25]$ ms) and one sample acquired with five diffusion encoding times ($\delta = 2.5$ ms, $\Delta = [5, 10, 15, 20, 25]$ ms). All diffusion weighted images were acquired with 8 b-values ($[70, 100, 200, \dots, 700] \text{ s mm}^{-2}$), and matrix size of $200 \times 44 \times 44$. The diffusion acquisition time was 2 hours 5 minutes for one diffusion time, 3 directions, 8 b-values. All acquisitions were acquired with a FOV of $10.4 \times 2.3 \times 2.3 \text{ mm}^3$. The average signal-to-noise ratios (SNRs) of the DW images were 31 at $b = 70 \text{ s mm}^{-2}$ and 13 at $b = 700 \text{ s mm}^{-2}$.

2.4. Image analysis

The $T_2\text{w}$ images were manually co-registered with the diffusion-weighted images. For each of the six imaged ganglia, several three dimensional ROIs were manually segmented slice by slice on the $T_2\text{w}$ image. We show in figure 2 the $T_2\text{w}$ image and the physical locations of 3

large cells ROIs from ganglion number 2. In total, we have selected for further analysis 21 ROIs of large cell neurons. The ROIs were manually segmented such that each ROI contains the voxels associated with only one neuron. We selected only the neurons that were clearly indentifiable on the $T_2\text{w}$ image based on the signal intensity, contrast, and the position within the ganglion (see diagram in figure 1).

The dMRI signals corresponding to the ROIs were processed to compute the experimental ADC using a linear fit of the logarithm of the signal versus the b-value. Even for large cell neurons, there might be, although less pronounced, some anisotropy due to the shape of the cells as well as the shape and position of the nucleus. For these reasons we averaged the ADC in the three directions, x , y , and z , to obtain the mean diffusivity, MD (Le Bihan *et al* 2001, Mori and Zhang 2009, Basser *et al* 1994, Kingsley 2006):

$$\text{MD} = \frac{\text{ADC}_x + \text{ADC}_y + \text{ADC}_z}{3}.$$

2.5. Simulations

The dMRI signal is the total transverse water proton magnetization at the echo time (TE). We simulated the transverse water proton magnetization by solving the Bloch-Torrey equation (Torrey 1956)

$$\begin{aligned} \frac{\partial}{\partial t} M(\mathbf{x}, t) = & -\gamma f(t) \mathbf{g} \cdot \mathbf{x} M(\mathbf{x}, t) \\ & + \nabla \cdot (D^l \nabla M(\mathbf{x}, t)), \quad \mathbf{x} \in \cup \Omega^l, \end{aligned} \quad (1)$$

where i is the imaginary unit, D^l is the intrinsic diffusion coefficient in the geometrical compartment Ω^l , and γ is the gyromagnetic ratio of the proton. The complex-valued magnetization $M(\mathbf{x}, t)$ is a function of position \mathbf{x} and time t , and depends on the diffusion-encoding gradient magnetic field $\mathbf{G}(t) = \mathbf{g}f(t)$. The amplitude and direction information of the diffusion-encoding gradient is contained in the vector $\mathbf{g} \in \mathbb{R}^3$ and the time profile of the effective gradient magnetic field is $f(t)$. For the PGSE sequence, the effective time profile is defined by:

$$f(t) = \begin{cases} 1 & 0 < t < \delta, \\ -1 & \Delta < t < \Delta + \delta, \\ 0 & \text{otherwise,} \end{cases}$$

where δ is the duration of the gradient pulses and Δ the delay between the start of the two pulses. The signal is measured at the echo time TE, with $2\delta \leq \text{TE} < 2\Delta$.

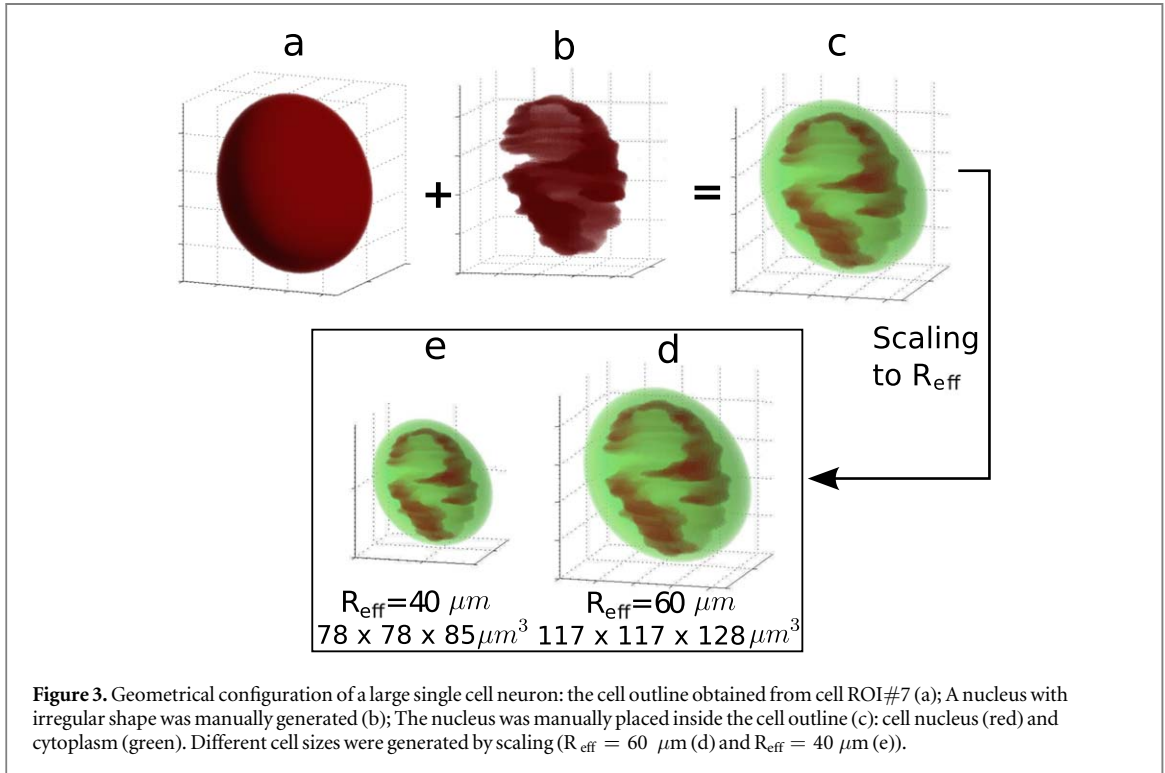
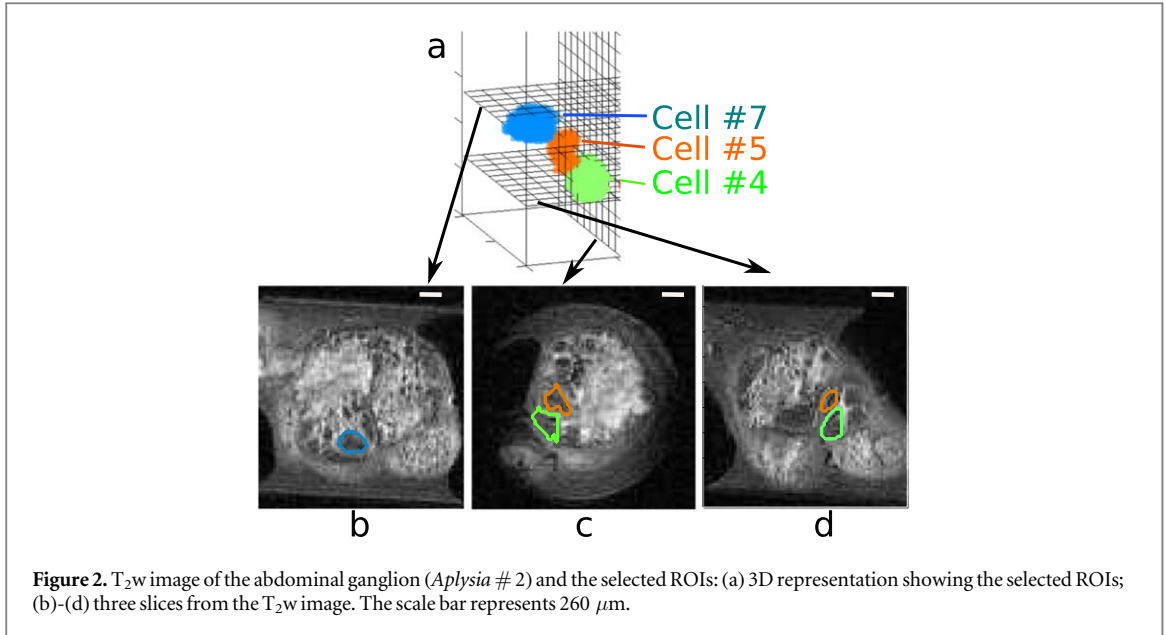
We solved the above equation subject to impermeable boundary conditions on $\partial \Omega^l$:

$$D^l \nabla M(\mathbf{x}, t) \cdot \nu = 0, \quad \mathbf{x} \in \partial \Omega^l, \quad (2)$$

where ν is the outward normal vector and imposed the initial condition:

$$M(\mathbf{x}, 0) = 1, \quad \mathbf{x} \in \Omega^l, \quad (3)$$

meaning uniform spin density in all Ω^l . The diffusion MRI signal is the integral of magnetization at TE:



$$S = \sum_l \int_{\mathbf{x} \in \Omega^l} M(\mathbf{x}, TE) d\mathbf{x}. \quad (4)$$

The numerical method for solving equations (1)–(3) was adapted from (Li *et al* 2013).

The b -value (Bihan *et al* 1986), in case of the PGSE sequence is:

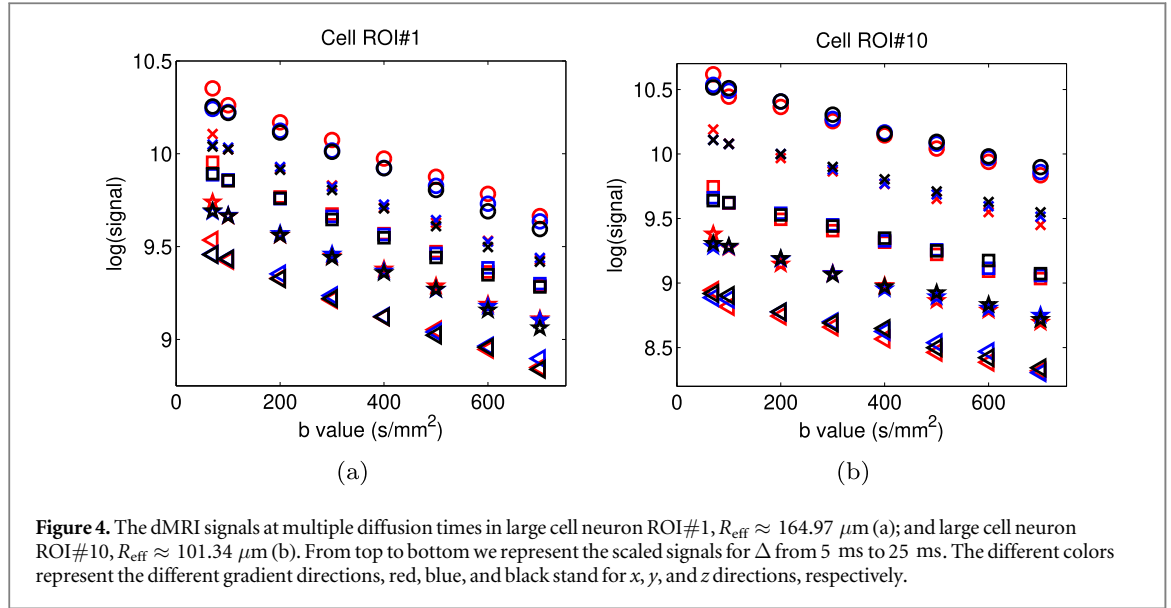
$$b(\mathbf{g}, \delta, \Delta) = \gamma^2 \|\mathbf{g}\|^2 \delta^2 (\Delta - \delta/3).$$

The ADC can be calculated as:

$$\text{ADC} = -\frac{\partial}{\partial b} \log \frac{S(b)}{S(0)} \Big|_{b=0}. \quad (5)$$

The ADC obtained from the numerically simulated dMRI signal was computed in the same way and using the same b -values as for experimental data.

In what follows we describe the geometrical configurations used in the simulations. To create computational domains in which to perform numerical simulations of large cell neurons, we segmented the cell outline of one particular large cell neuron. This cell outline (denoted by Ω_{cell}) was segmented from the anatomical T₂w image of the large neuron ROI (see figure 3(a)) and was used for all simulations of large cell neurons. We note that Ω_{cell} is a slightly elongated



ellipsoid. In addition, we created by hand several examples of irregularly shaped nuclei, Ω_n , as in figure 3(b). The shape of the nucleus was inspired by the high resolution images in (Lee *et al* 2015). The generated Ω_n , when placed inside Ω_{cell} , takes up between 25%–30% volume fraction. Even though not visible in the T_2w images, there may be a small volume (up to 5%) of satellite cells (very small cells, $3\mu\text{m}$ maximum radius, without nucleus (Conn and Kaczmarek 1989, Musio and Bedini 1990, Lee *et al* 2015)) surrounding the single cell neurons. However, since the volume of the satellite cells is small and to simplify the study, we did not include the satellite cells in the simulations.

By placing Ω_n in Ω_{cell} we obtained several geometrical configurations. To take into account the effect of the size of the cells on the ADC, we simply scaled the reference geometry such that Ω_{cell} had the desired total volume, leading to effective cell radii ranging from $100 \mu\text{m}$ to $210 \mu\text{m}$ (figure 3).

The simulated dMRI signal for the large cell neurons can be generated by solving the Bloch-Torrey equations in Ω_{cell} with two compartments: the nucleus Ω_n and the cytoplasm $\Omega_c = \Omega_{\text{cell}} - \Omega_n$. The intrinsic diffusivities in the cytoplasm and nucleus, D_c and D_n , respectively, were chosen to range from $0.5 \mu\text{m}^2/\text{ms}$ to $2.4 \mu\text{m}^2/\text{ms}$ as described in the literature (Lee *et al* 2015). The total signal in a large cell neuron is:

$$S_{\text{cell}} = (1 - v_n)S_c + v_n S_n, \quad (6)$$

where v_n is the volume fraction of the nucleus, S_c and S_n are the signals in the cytoplasm and the nucleus, respectively.

2.6. Analytical formula of the ADC in short diffusion time regime

A well-known formula for the ADC in the short diffusion time regime is the following short time approximation (STA) (Mitra *et al* 1992, 1993):

$$ADC_{\text{STA}} = D_0 \left(1 - \frac{4\sqrt{D_0}}{3 \dim \sqrt{\pi}} \sqrt{\Delta} \frac{S}{V} \right), \quad (7)$$

where $\frac{S}{V}$ is the surface to volume ratio and D_0 is the intrinsic diffusivity coefficient. In the above formula the pulse duration δ is assumed to be very small compared to Δ . A recent correction to the above formula, taking into account the finite pulse duration δ (Schiavi *et al* 2016) is the following:

$$ADC_{\text{STA}} = D_0 \left[1 - \frac{4\sqrt{D_0}}{3 \dim \sqrt{\pi}} C_{\delta, \Delta} \frac{S}{V} \right], \quad (8)$$

where

$$C_{\delta, \Delta} = \frac{4(\Delta + \delta)^{7/2} + (\Delta - \delta)^{7/2} - 2(\delta^{7/2} + \Delta^{7/2})}{35 \delta^2 (\Delta - \delta/3)} \quad (9)$$

$$= \sqrt{\Delta} \left(1 + \frac{1}{3} \frac{\delta}{\Delta} - \frac{8}{35} \left(\frac{\delta}{\Delta} \right)^{3/2} + \dots \right). \quad (10)$$

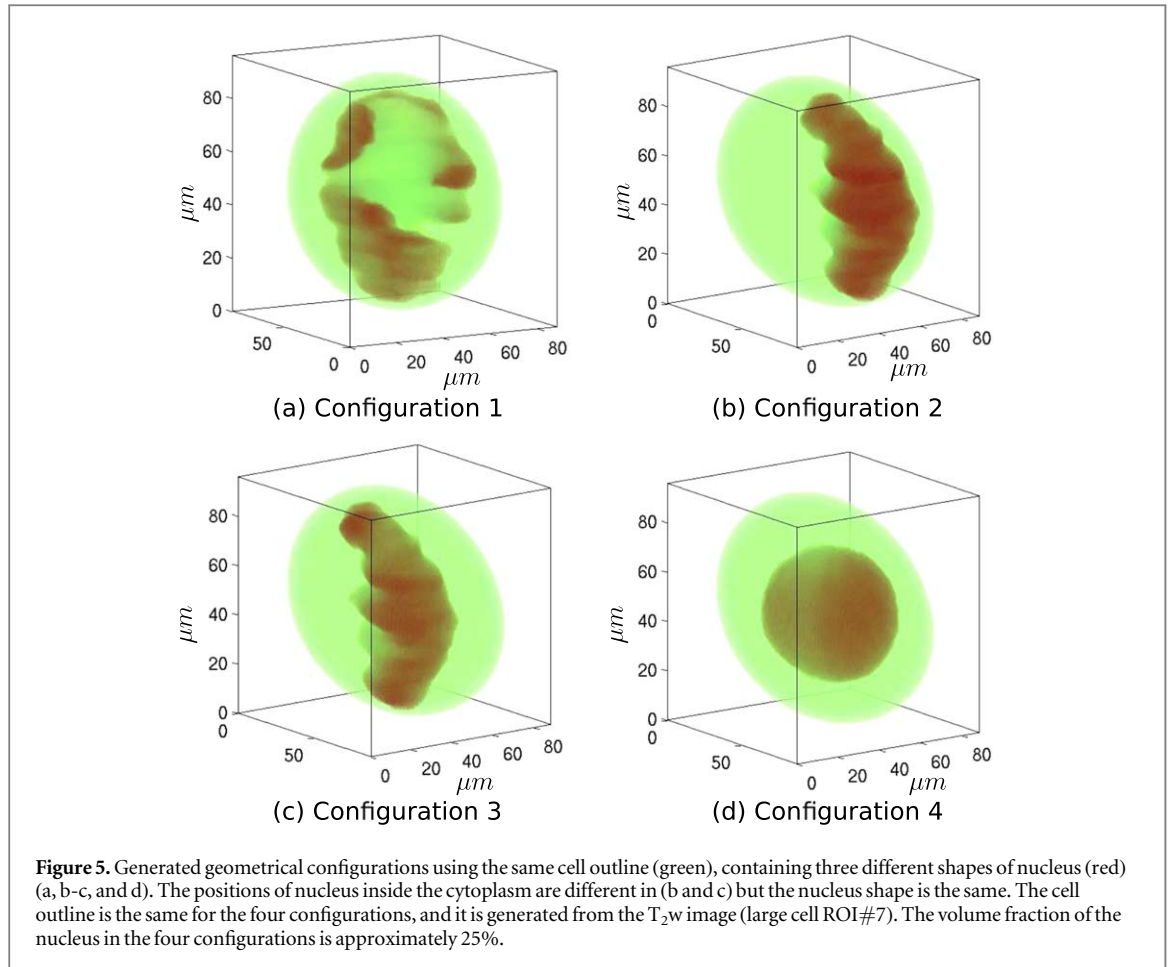
When $\delta \ll \Delta$, the value $C_{\delta, \Delta}$ is approximately $\sqrt{\Delta}$.

3. Results

3.1. Experimental time-dependent ADC

The experimental dMRI signals at multiple diffusion times in the large cell neuron ROIs are shown in figure 4. It is clear that in the range of b -values used here, from 70 to 700 s mm^{-2} , the logarithm of the signal is a linear function of b -value, meaning that the ADC is sufficient to describe the signal in this range. Higher order effects such as a Kurtosis (Chabert *et al* 2005, Fröhlich *et al* 2006, Jensen *et al* 2005, Jensen and Helpert 2010) term need not be considered. Moreover, the signals in the x , y , and z directions do not show significant anisotropy.

The time-dependent ADC measured over the 21 ROIs of large cell neurons are shown in table 1. We found that, when the diffusion time is increased from



5 to 25 ms, the average experimental ADC drops by 9.45% in large cell neurons.

3.2. Validation of the STA by numerical simulations in large cell neurons

Assuming a free diffusivity of $2.00 \mu\text{m}^2/\text{ms}$, the average diffusion displacement is between 7.7 and $17.3 \mu\text{m}$ for the diffusion times between 5 and 25 ms. From the point of view of diffusing water molecules, the diffusion displacement is much smaller than the size of the large cell neurons. Hence, we should be able to apply the mathematical model ADC_{STA} to the measured ADC in the large cell neurons. Nevertheless, we first used numerical simulations to compare the simulated ADC with ADC_{STA} (specifically, we used equation (8)).

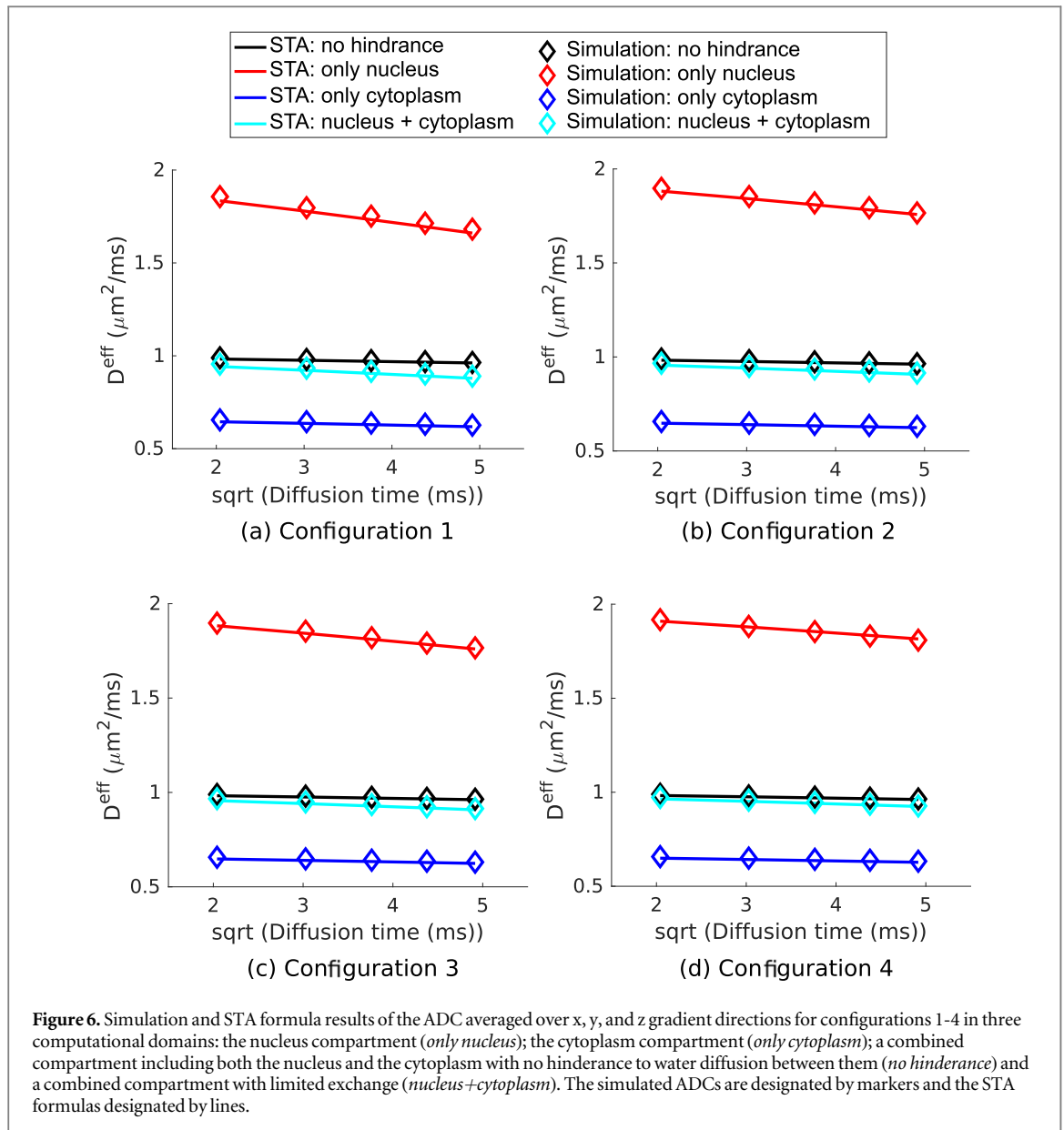
We constructed several geometrical configurations for the large cell neurons, consisting of a nucleus and surrounding cytoplasm, based on three types of nucleus shapes and positions of the nucleus inside the cell, as shown in figure 5.

To perform simulations, we scaled the configurations 1-4 (figure 5) so that they each have the effective radius of $100 \mu\text{m}$. We referred to information from published literature (Lee *et al* 2015) to choose reasonable biological parameters: $D_c = 0.67 \mu\text{m}^2/\text{ms}$ and $D_n = 2 \mu\text{m}^2/\text{ms}$.

Table 1. Mean and standard deviations (SD) of experimental ADCs in large cell neurons ROIs ($N = 21$). The average ADCs were observed to drop by 9.45%.

Δ (ms)	Mean ($\mu\text{m}^2/\text{ms}$)	SD ($\mu\text{m}^2/\text{ms}$)
5	0.974	0.096
7.5	0.957	0.085
10	0.938	0.087
12	0.915	0.080
15	0.914	0.080
20	0.897	0.081
25	0.882	0.087
Drop	9.45%	

We solved the Bloch-Torrey equation for configurations 1-4 in each of the following three domains to obtain the simulated ADC at diffusion times between 5 ms and 25 ms. In figure 6 we show the averaged diffusion time dependent ADC over x , y , and z gradient directions for: a) the nucleus compartment only (*only nucleus*); b) the cytoplasm compartment only (*only cytoplasm*); c) a combined compartment including both the nucleus and the cytoplasm with no hindrance to water diffusion between them (*no hindrance*); d) a combined compartment including the nucleus and the cytoplasm with limited exchange for which we computed the ADC as the weighted average of the



ADCs in nucleus and cytoplasm (*nucleus+cytoplasm*). The close agreement between the numerically simulated ADC and the STA formula is clear for all 3 computational domains in the 4 geometrical configurations. Therefore, we are justified in using the STA formula to compare with the experimental ADC for large cell neurons instead of running further numerical simulations.

We note that the averaged-ADC drop of the combined nucleus and cytoplasm (no hinderance) between $\Delta = 5$ ms and $\Delta = 25$ ms is under 2.5% for all four configurations (both STA and simulation), whereas the weighted average of the STA ADC of the nucleus and cytoplasm compartments with limited exchange (*STA: nucleus+cytoplasm*) drops by 6.7% for configuration 1, by 5.1% for configurations 2 and 3, and by 4.1% for configuration 4. Moreover, the weighted average of the simulated ADC for this domain (*Simulation: nucleus+cytoplasm*) drops by

6.8% for configuration 1, by 5.4% for configurations 2 and 3, and by 4.7% for configuration 4. Let us now compare these values with experimental results we described earlier: when the diffusion time is increased from 5 to 25 ms, the average experimental ADC drops by 9.45% in large cell neurons. To achieve the larger ADC drop of the experimental data using numerical simulations, we would need to increase the surface to volume ratios of the two compartments. However, it is extremely difficult to manually adjust the finite element mesh to increase the surface to volume ratios. This requires moving the points of the finite element mesh manually, while satisfying constraints on the compartment volume fractions, the nuclear volume fraction being between 25% and 30% (Jelescu 2013, Lee *et al* 2015). For this reason, once we have established the validity of the STA formula as a good approximation to the simulated ADC at $R_{\text{eff}} \geq 100\mu\text{m}$, we will use the STA formula instead

Table 2. Results obtained by fitting the experimental ADC(Δ) with equation (8) ($ADC = AC_{\delta,\Delta} + B$) for 21 large cell neuron ROIs. The effective radius (R_{eff}) of each cell was estimated from the T_2w image. The estimated cell radius (R_{est}) was found by using equation (13).

ROI#	R_{eff} (μm)	A ($\mu\text{m}^2/\text{ms}^{3/2}$)	B ($\mu\text{m}^2/\text{ms}$)	R_{est} (μm)
1	101.3	-0.063 4	1.212	15.8
2	109.6	-0.035 1	1.218	28.8
3	113.9	-0.016 5	0.983	44.6
4	115.4	-0.026 7	0.982	27.4
5	115.8	-0.025 5	1.039	31.3
6	121.2	-0.060 0	1.150	15.5
7	126.0	-0.057 4	1.111	15.3
8	126.3	-0.043 3	1.032	18.2
9	129.6	-0.065 7	1.253	16.1
10	130.4	-0.024 4	0.953	28.7
11	134.2	-0.029 6	1.113	29.8
12	140.7	-0.033 3	0.967	21.5
13	149.7	-0.054 3	0.980	13.5
14	150.4	-0.032 1	1.051	25.2
15	151.8	-0.035 4	1.186	27.5
16	155.7	-0.031 0	1.040	25.8
17	160.5	-0.020 6	1.059	39.8
18	160.5	-0.028 4	0.970	25.3
19	162.6	-0.017 9	1.085	47.4
20	165.0	-0.014 5	1.042	55.1
21	207.8	-0.012 1	0.857	49.2

of the simulated ADC, since we can easily adjust the surface to volume ratios in the STA formula without constructing a finite element mesh.

We see that the two compartment (nucleus and cytoplasm) with limited exchange computational domain is the best description of the diffusion in the large cell neurons among the four domains considered and that a more irregular nucleus results in a larger ADC drop. We now expand on these ideas using the STA formula.

3.3. Comparing the STA formula with the experimental ADC for large cell neurons

3.3.1. One compartment STA model

If the hindrance to water diffusion between the two compartments can be neglected, then the nucleus and the cytoplasm can be combined into one compartment, with a single diffusion coefficient. This corresponds to the simulations performed in the third computational domain (the combined compartment). From the experimental ADC, by fitting $ADC = AC_{\delta,\Delta} + B$ using equation (8), we can find the coefficients A and B , from which the surface to volume ratio can be obtained:

$$A = -B \frac{4\sqrt{D_0}}{3 \dim \sqrt{\pi}} \frac{S}{V}, \quad B = D_0. \quad (11)$$

If we further assume the shape is a sphere, then

$$A = -B \frac{4\sqrt{D_0}}{3\sqrt{\pi}} \frac{1}{R}, \quad B = D_0, \quad (12)$$

from which an estimated cell radius can be obtained. Note that the cell neuron outlines are actually not spherical, and the quantity S/V depends on the size and the shape of the cell neuron outlines. However, we prefer to use the quantity *effective radius* which is more intuitive and familiar than the quantity S/V .

We denote by

$$R_{\text{est}} = -D_0 \frac{4\sqrt{D_0}}{3\sqrt{\pi}} \frac{1}{A}, \quad (13)$$

the estimated cell radius determined by applying the STA formula to the experimental ADC. The idea is to compare the R_{est} with the visually obtained effective radius, denoted R_{eff} , of the 21 large cell ROIs. The results are shown in table 2. It is clear that the cell size is severely underestimated: R_{est} is on average only 25% of R_{eff} . This suggests that a one compartment model is not sufficient to describe the diffusion in the large cell neurons of the *Aplysia*, which is a conclusion we already alluded to in the previous section.

3.3.2. Two compartment STA model

When the cell is made up of different components such as cytoplasm and nucleus, under the short diffusion time and low b-value regime, the water exchange between the cytoplasm and the nucleus can be assumed to be limited enough so that the water exchange does not affect the ADC, then the ADC is the weighted average of the ADC in the individual compartments:

$$ADC_{STA}^{2cmt} = (fD_n + (1-f)D_c) - \frac{4}{3 \dim \sqrt{\pi}} \left(\frac{S_n}{V} D_n^{3/2} + \frac{S_c}{V} D_c^{3/2} \right) C_{\delta, \Delta}, \quad (14)$$

where $f = \frac{V_n}{V}$ is nucleus volume fraction, D_n and D_c are the intrinsic diffusivity coefficients of nucleus and cytoplasm components, $\frac{S_n}{V_n}$ and $\frac{S_c}{V_c}$ are the surface by volume ratios for the nucleus and cytoplasm components.

The quantities $\frac{S_n}{V}$ and $\frac{S_c}{V}$ are related to the shape and size of the nucleus and the cell outline. The outline of the large cell neurons can be seen on the T_2w images to be spheroid or somewhat ellipsoid. Recall that the volume fraction of the nucleus is f . It is easy to show that if the nucleus and the large cell neuron outline are spheres, then

$$\frac{S_n}{V} = 3 \frac{f^{2/3}}{R_{eff}}, \quad \text{and} \quad \frac{S_c}{V} = \frac{S_n}{V} + 3 \frac{1}{R_{eff}}. \quad (15)$$

The shape of the nucleus inside the cell cannot be seen on the T_2w images. Therefore, we referred to the information from published literature (Lee *et al* 2015) to manually construct a three-dimensional configuration consisting of an irregularly shaped nucleus placed inside an ellipsoid (see Configuration 1, figure 5(a)). For this configuration, we numerically computed the surface to volume ratios:

$$\frac{S_n}{V} = 8.1196 \frac{f^{2/3}}{R_{eff}}, \quad \text{and} \quad \frac{S_c}{V} = \frac{S_n}{V} + 4.539 \frac{1}{R_{eff}}. \quad (16)$$

We then manually constructed another irregularly shaped nucleus (Configuration 2, figure 5(b)) and numerically computed the surface to volume ratios:

$$\frac{S_n}{V} = 6.053 \frac{f^{2/3}}{R_{eff}}, \quad \text{and} \quad \frac{S_c}{V} = \frac{S_n}{V} + 4.539 \frac{1}{R_{eff}}. \quad (17)$$

For Configuration 3 (see figure 5(c)), we simply moved the nucleus with respect to Configuration 2, therefore, the above surface to volume ratios stay the same. Finally, a third nucleus shape (essentially an ellipsoid) was constructed manually (Configuration 4, figure 5(d)) and the numerically computed ratios are:

$$\frac{S_n}{V} = 4.5894 \frac{f^{2/3}}{R_{eff}}, \quad \text{and} \quad \frac{S_c}{V} = \frac{S_n}{V} + 4.539 \frac{1}{R_{eff}}. \quad (18)$$

It is easy to show that the shapes of the large neuron cell outline and the nucleus affect the surface to volume ratios through the parameters Q_1 and Q_2 :

$$\frac{S_n}{V} = Q_1 \frac{f^{2/3}}{R_{eff}}, \quad \text{and} \quad \frac{S_c}{V} = \frac{S_n}{V} + Q_2 \frac{1}{R_{eff}}. \quad (19)$$

The parameter Q indicate the *non-smoothness* of the shape, for a sphere, $Q = 3$, for the ellipsoids we generated, $Q \approx 4.5$, the more irregular the shape, the higher the Q . The nucleus shape that corresponds the best to the literature reports (Lee *et al* 2015) about *Aplysia* neurons is in Configuration 1, where $Q = 8.1$.

Now, we state the two compartment STA model:

$$ADC_{STA}^{2cmt} = -\frac{4}{3 \dim \sqrt{\pi}} [Q_1 f^{2/3} (D_n^{3/2} + D_c^{3/2}) + Q_2 D_c^{3/2}] \frac{1}{R_{eff}} C_{\delta, \Delta} + [fD_n + (1-f)D_c], \quad (20)$$

which we will apply to the experimental ADC. This can be stated as a linear regression problem:

$$y = \tilde{c}_0 - \tilde{c}_1 \tilde{x}, \quad (21)$$

where the dependent variable $y = ADC_{STA}^{2cmt}$ is the diffusion time-dependant ADC, and the independent variable is $\tilde{x} = \frac{1}{R_{eff}} C_{\delta, \Delta}$.

First we combined the data from 21 ROIs and the multiple diffusion times to solve one regression problem and obtained the following fitted values:

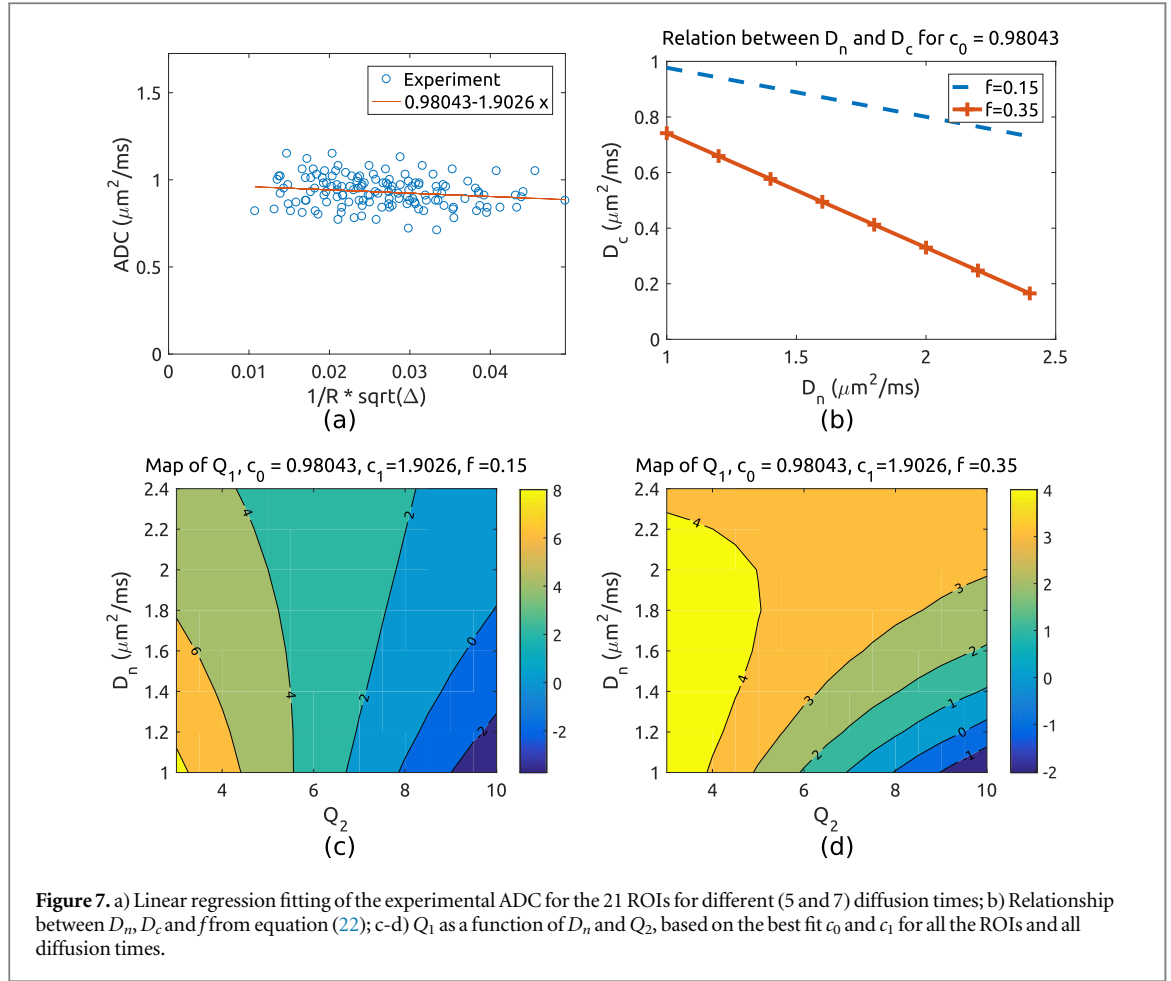
$$\tilde{c}_0 = [fD_n + (1-f)D_c] = 0.98043, \quad (22)$$

$$\tilde{c}_1 = \frac{4}{3 \dim \sqrt{\pi}} [Q_1 f^{2/3} (D_n^{3/2} + D_c^{3/2}) + Q_2 D_c^{3/2}] = 1.9026, \quad (23)$$

where the numerical fitting is shown in figure 7(a). From equation (22) we plot the relationship between D_n , D_c and f for plausible choices of f (between 0.15 and 0.35, see figure 7(b)). We see an inverse relationship between D_c and D_n and this inverse relationship is steeper at higher f . This also helps us bound reasonable values of D_n , since D_c should not be too small.

In the following, we will limit D_n to the range $D_n \in [1, 2.4] \mu\text{m}^2/\text{ms}$. We plot the relationship between Q_1 and $\{D_n, Q_2\}$, where $D_n \in [1, 2.4] \mu\text{m}^2/\text{ms}$, $Q_2 \in [3, 10]$. We recall that $Q_2 = 3$ implies a spherical shape of the cell outline, and $Q_2 = 4.5$ implies an ellipsoid shape. The higher the value, the more irregular the shape. We choose two values of f ($f = 0.15$ and $f = 0.35$) subject to the constraints in equations (22)–(23). The resulting values for Q_1 are shown in contour plots in Figs. 7(c)–(d).

Since the large cell neuron outline has an ellipsoid shape, we can assume that $Q_2 \approx 4.5$. When $f = 0.15$ (figure 7(c)), looking at the line $Q_2 = 4.5$, we see the range for Q_1 is between 4 and 5, which is too low, given the information from the literature on the shape of the nucleus (much more irregular than an ellipsoid). At $f = 0.35$ (figure 7(d)), the range of Q_1 is even lower, less than 4. Therefore, it is clear that there are some inaccuracies in the above fitting procedure. We



suspect that this is due to the noise in the measured ADCs as well as to errors in the estimated radii of the cells (which was done manually).

To compensate for the error and uncertainty in the ADCs and the cell radii, we next solved the linear regression problem for each ROI separately:

$$y = c_0^i - c_1^i x, \quad (24)$$

where the dependent variable $y = ADC_{STA}^{2cmpt}$ is the diffusion time-dependant ADC, and the independant variable is $x = C_0 \Delta$. This way, we obtain 21 values of c_0^i and 21 values of c_1^i . The fitted values will be then:

$$c_0^i = [fD_n + (1 - f)D_c], \quad (25)$$

$$c_1^i = \frac{4}{3 \dim \sqrt{\pi}} \times [Q_1 f^{2/3} (D_n^{3/2} + D_c^{3/2}) + Q_2 D_c^{3/2}] / R_{eff}^i, \quad (26)$$

where we expect inaccuracies in R_{eff}^i . Therefore, we set the fitting error of c_0^i (equation (25)) to zero and obtain D_c^i as a function of the continuous variables f and D_n :

$$D_c^i(f, D_n) = \frac{c_0^i - fD_n}{1 - f}.$$

On the other hand, we will not set equation (26) to zero, because we expect the fitting errors (normalized below),

$$Err^i(f, Q_1, D_n, Q_2) = \left| \frac{4}{3 \dim \sqrt{\pi} c_1^i R_{eff}^i} [Q_1 f^{2/3} (D_n^{3/2} + D_c^i(f, D_n, c_0^i)^{3/2}) + Q_2 D_c^i(f, D_n, c_0^i)^{3/2}] - 1 \right|,$$

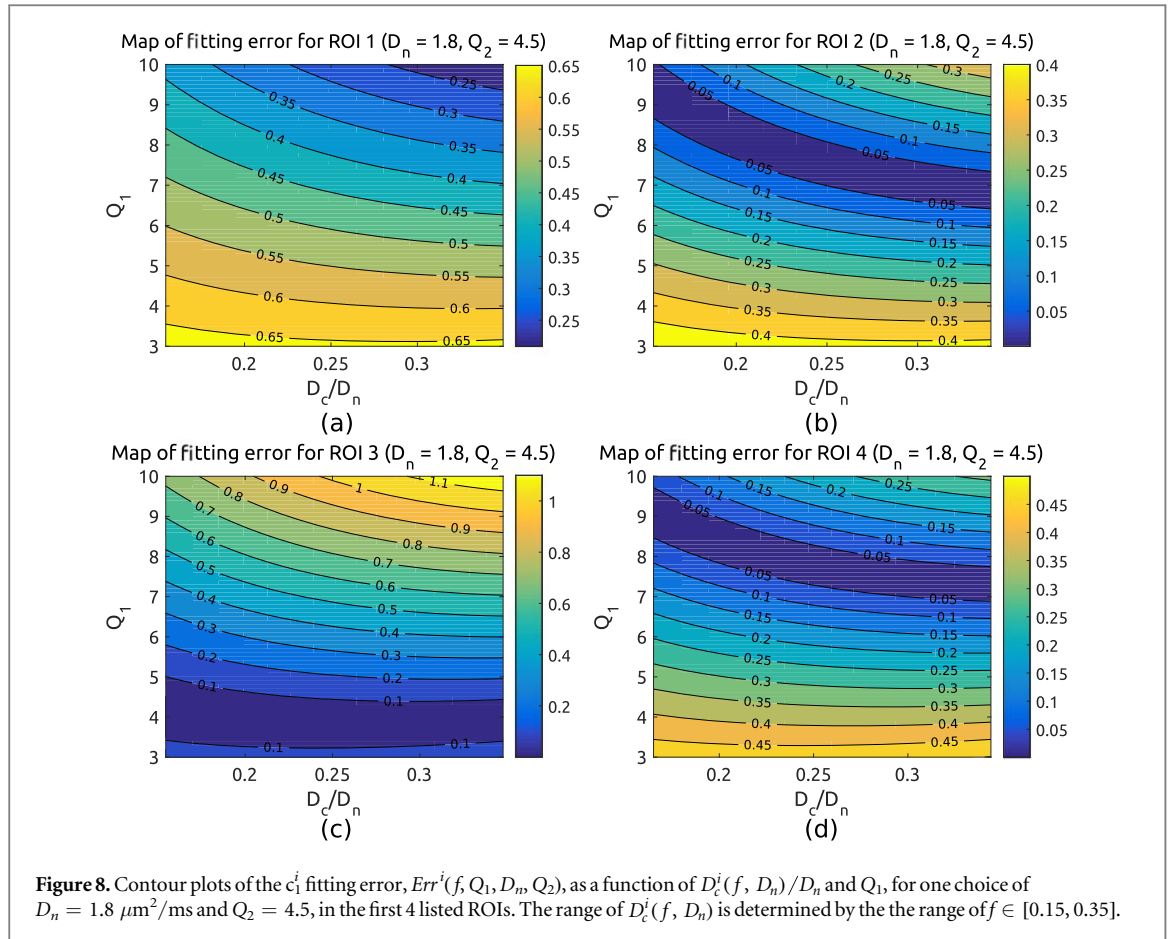
$i = 1, \dots, 21$, will not reach zero due to the inaccuracies in R_{eff}^i (and the ADC). Knowing that the physically plausible values of f should stay in the range $0.15 \leq f \leq 0.35$, we plot in figure 8 the c_1^i fitting error, $Err^i(f, Q_1, D_n, Q_2)$, as a function of $D_c^i(f, D_n)/D_n$ and Q_1 , for one choice of $D_n = 1.8 \mu m^2/ms$ and $Q_2 = 4.5$, in the first 4 listed ROIs. The range of $D_c^i(f, D_n)$ in figure 8 is determined by the the range of $f \in [0.15, 0.35]$. It can be seen that $Err^i(f, Q_1, D_n, Q_2)$ is much more dependent on Q_1 than on D_c (and hence f). This observation holds in general in the range of D_n and Q_2 of interest. Therefore, in searching for Q_1 , we will first remove its dependence on f by averaging $Err^i(f, Q_1, D_n, Q_2)$ over all $f \in [0.15, 0.35]$.

We now proceed to find Q_1 that solves the following minimization problem over all the ROIs:

$$Q_1^{\min}(D_n, Q_2) = \min_{Q_1} E^{total}(Q_1, D_n, Q_2),$$

$$E^{total}(Q_1, D_n, Q_2) \equiv \sum_{i=1 \dots 21} E^i(Q_1, D_n, Q_2), \quad (27)$$

where the averaged (over $f \in [0.15, 0.35]$) fitting error for each ROI is defined as:



$$E^i(Q_1, D_n, Q_2) := \frac{1}{0.35 - 0.15} \int_{f=0.15}^{f=0.35} \left| \frac{4[Q_1 f^{2/3}(D_n^{3/2} + D_c^i(f)^{3/2}) + Q_2 D_c^i(f)^{3/2}]}{3 \dim \sqrt{\pi} c_1^i R_{\text{eff}}^i} - 1 \right| df.$$

The solution to the minimization problem in equation (27) depends on the parameters D_n and Q_2 , but not on f and D_c . We make this clear by using the notation $Q_1^{\min}(D_n, Q_2)$.

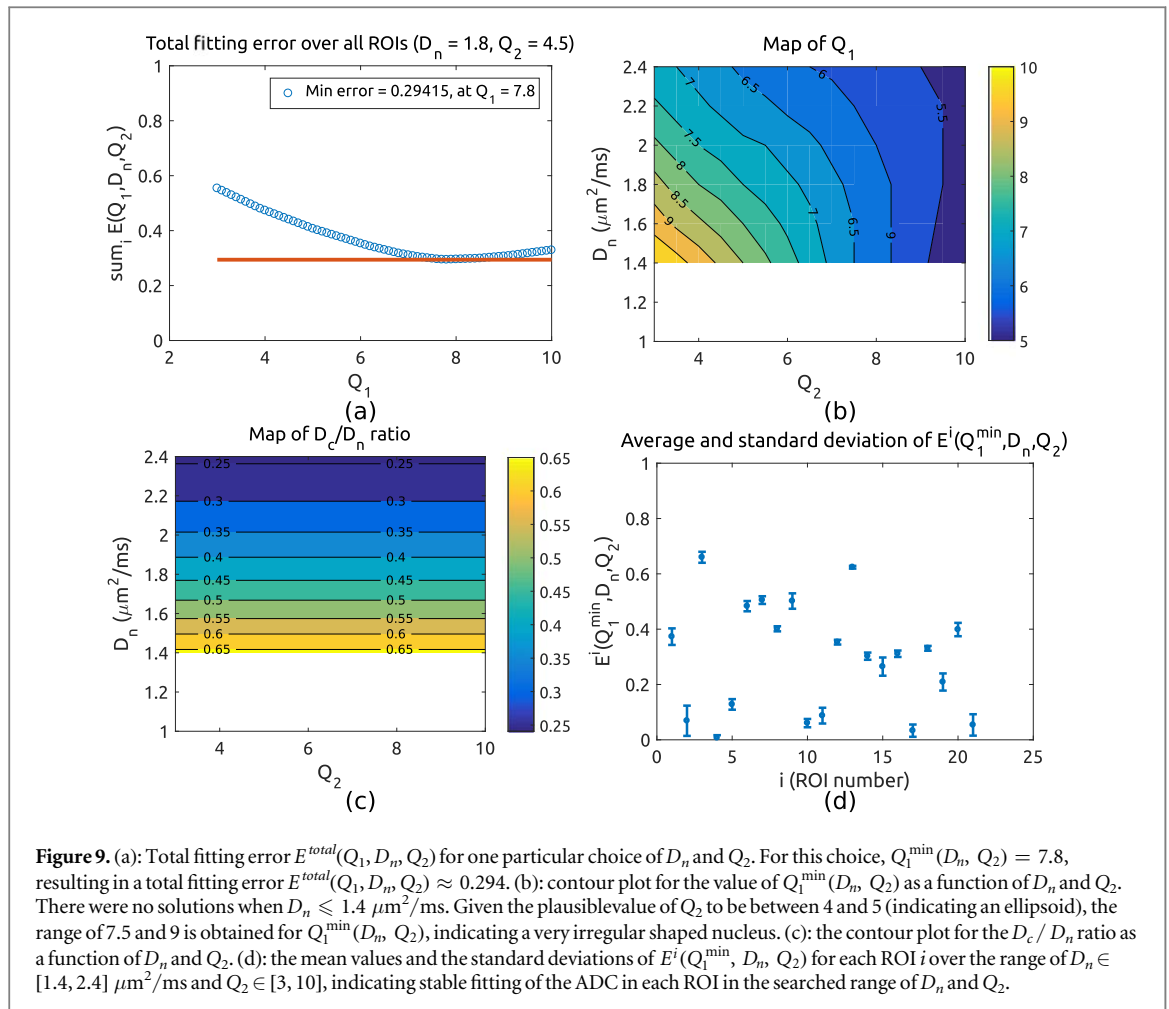
In figure 9(a) we show the total fitting error $E^{\text{total}}(Q_1, D_n, Q_2)$ for one particular choice of D_n and Q_2 , and for this choice, $Q_1^{\min}(D_n, Q_2) = 7.8$, resulting in the total fitting error $E^{\text{total}}(Q_1, D_n, Q_2) \approx 0.294$. We then do an exhaustive search in $D_n \in [1, 2.4] \mu\text{m}^2/\text{ms}$ and $Q_2 \in [3, 10]$. We show in figure 9(b) the contour plot for the value of $Q_1^{\min}(D_n, Q_2)$. We found no solutions when $D_n \leq 1.4 \mu\text{m}^2/\text{ms}$ and we found the range of $Q_1^{\min}(D_n, Q_2)$ to be between $5 \leq Q_1^{\min}(D_n, Q_2) \leq 10$ given the ranges $D_n \in [1.4, 2.4] \mu\text{m}^2/\text{ms}$ and $Q_2 \in [3, 10]$. If we take as plausible the value of Q_2 to be between 4 and 5 (indicating an ellipsoid) and the value of D_n to be between $1.4 \mu\text{m}^2/\text{ms}$ and $1.8 \mu\text{m}^2/\text{ms}$, we get a range of between 7.5 and 9 for $Q_1^{\min}(D_n, Q_2)$, indicating a very irregular shaped nucleus, in agreement with the literature (Lee *et al* 2015). We show in figure 9(c) the contour plot of the D_c/D_n ratio as a function of D_n and Q_2 . For plausible values of Q_2 , between 4 and 5, and of D_n , between $1.4 \mu\text{m}^2/\text{ms}$ and $1.8 \mu\text{m}^2/\text{ms}$, this ratio is

between 0.45 and 0.65, again in agreement with the literature.

Finally, in figure 9(d) we plot the mean values and the standard deviations of $E^i(Q_1^{\min}, D_n, Q_2)$ for each ROI i over the ranges of $D_n \in [1.4, 2.4] \mu\text{m}^2/\text{ms}$ and $Q_2 \in [3, 10]$ searched. This shows that the obtained minimum fitting error in each ROI is stable across the searched space of D_n and Q_2 .

The fact that we found no solutions for $D_n < 1.4$ means that $D_n \geq 1.4 \mu\text{m}^2/\text{ms}$, which is a range of D_n that is consistent with the literature reports on the nucleus ADCs in *Aplysia* neurons (Schoeniger *et al* 1994, Grant *et al* 2001). The nucleus diffusivity is known to be high compared to the cytoplasm diffusivity. It was not obvious from the outset that we would be able to pinpoint D_n to be no smaller than $1.4 \mu\text{m}^2/\text{ms}$. This came out merely from insisting on the nucleus shape parameter Q_1 to be between 3 and 10.

In addition, because we know that big cell neurons are certainly ellipsoid in shape, we were able to constrain the possible values of Q_2 . This constraint in turn allowed us to conclude that Q_1 is between 7.5 and 9, which is a reasonable range for an irregular nucleus



shape. Without formulating the linear regression problem for each ROI separately, as we described above, the obtained Q_1 would be less than 5, which is much too low to be true.

4. Discussion

To study the diffusion time dependence of the dMRI signal and evaluate if measurements at multiple diffusion times can give additional information about the tissue microstructure, we imaged the *Aplysia* abdominal ganglia at high resolution and several diffusion times. Given the very long experimental times, we used chemically-fixed samples. However, one should keep in mind that the aldehyde fixatives used may significantly alter tissue MRI properties. Shepherd and colleagues reported in (Shepherd *et al* 2009) that the rat cortical slices fixed by immersion in 4% formaldehyde solution demonstrated 21% and 81% reductions in tissue T_1 and T_2 , respectively. By washing fixed tissues with PBS to remove free formaldehyde solution T_2 can be recovered. In addition, the membrane permeability was increased after fixation with 4% formaldehyde (Shepherd *et al* 2009). However, we find it a worthwhile trade-off since cell (sub-)structures are mostly preserved in the fixation

process and this allows us to obtain high resolution data at multiple diffusion times for which *in-vivo* or fresh tissue imaging would not be possible.

We have acquired and analyzed the diffusion time-dependent dMRI data in the *Aplysia* neuronal network for large cell neurons. The time-dependent ADC at diffusion times ranging from $\Delta = 5$ ms to $\Delta = 25$ ms were presented. In the spirit of using the *Aplysia* as a biological phantom for diffusion MRI we conducted an analytical and numerical study in the case of the large cell neurons. The cell outline of these large neurons can be seen in the T_2 -weighted images, giving a reliable (but still approximate) estimate of the cell size. We chose to sum up the signal values over all the pixels of a manually generated ROI that contains one individual neuron, instead of using it at pixel level, in order to approach the experimental conditions in mammalian neuro-imaging where the cells are contained entirely in one voxel. By retaining only one cell in the ROI, we eliminate much of the uncertainty regarding the geometry of the diffusion medium being imaged. We know that the signal comes from the segmented cell and we know the size of the segmented cell up to some level of error. This is what we mean by a ‘biological phantom’.

This phantom retains much of the complexity of the cellular make-up (nucleus, cytoplasm) that is also

relevant to mammalian neuro-imaging while reducing the uncertainty about the cellular size. For example, we addressed the question of whether the nucleus and the cytoplasm should be modeled as two separate diffusion compartments, at least in the short diffusion time regime which is the case for large cell neurons in our experiments. We showed that indeed, two compartment diffusion fits the data better than combining them into a single diffusion compartment. Using the one compartment STA model resulted in a serious under-estimation of the cell size. This is relevant for mammalian imaging as the neurons have similar cellular make-up as the *Aplysia*, only smaller in size. Thus, for short time diffusion imaging (using oscillating gradients, for example), our results suggest that some modeling error could be due to the presence of the nucleus, since often diffusion in the soma is modeled by one compartment diffusion for mammalian neuro-imaging studies. Supported by numerical simulations and after taking into account the noise in the experimental ADC as well as the uncertainty in cell size due to manual segmentation, we established that a two compartment STA model is adequate to explain the behavior of the experimentally obtained ADC. This result also suggests that dMRI may be potentially used to probe the shape of the cell nucleus, which could be indicative of certain cellular abnormalities (Webster *et al* 2009).

Additionally, we showed that even if one has some information regarding the geometry of the cells being imaged, as we do for the *Aplysia* neurons, it is important to account for the uncertainty in the prior knowledge (in our case, the size of the cells from manual segmentation). We propose fitting the intended model individually to each neuron instead of using averaged quantities. While this is somewhat counter-intuitive since one would have assumed that averaging over all the large cell neurons would reduce noise in the model fitting procedure, we showed that this is not the case for the fitting of the two compartment short-time ADC model, and we suspect this is due to the error in the estimated cell size from the segmentation procedure.

We produced numerical simulations that showed the two compartment STA model is a valid approximation during the diffusion times ranging from $\Delta = 5$ ms to $\Delta = 25$ ms for large cells ($R_{\text{eff}} \geq 100 \mu\text{m}$). The use of the STA formula where one can tune the volume fractions of the nuclear and cytoplasm compartments as well as their surface to volume ratios increases the types of geometries that are accessible to modeling, in particular, those geometries for which the generation of finite element meshes would be very difficult.

In our work, we considered low b-values at multiple diffusion times to capture the large length scale geometrical structure information about the large neurons of the *Aplysia*. At the smaller length scales of mammalian cells, it would be important to consider higher b-values and possibly fitting non-linear models such as in (Ingo *et al* 2014, Gatto *et al* 2019).

In this study, we modeled the cellular and nuclear membranes as impermeable interfaces and represented the diffusion in each compartment by a diffusion coefficient, D_c and D_n , respectively. This is a simplification. Knowledge about the intra-cellular and intra-nuclear structures may be incorporated into the model if they become available. For example, the neurofilamentary structure of the giant axon of the squid was studied in (Beaulieu and Allen 1994) and found to result in an anisotropic diffusion ratio of 1.2 ± 0.1 . Membrane permeability, for example, may start to play a role at higher b-values and longer diffusion times beyond the regime where the STA model is valid. In the future, the intracellular vesicular and membrane-based organelles may be considered as well. We mention that the influence of different intracellular proteins and cell pathologies in mammalian cells have been studied and reviewed in (Colvin *et al* 2011, Harkins *et al* 2009, Matsumoto *et al* 2009, Sotak 2004).

Given the importance of the morphological features of the cellular nucleus in this study, the addition of higher magnification histology and nuclear counterstaining with 3D reconstruction could help to obtain better ground truth information of the real geometrical contribution of the neuronal nucleus to the dMRI signal, and would be a useful future direction to explore.

5. Conclusions

We have acquired and analyzed the diffusion time-dependent dMRI data in the *Aplysia* neuronal network for large cell neurons. We found that it is not sufficient to approximate the ADC using a one compartment short time approximation (STA) model. Using the one compartment STA model resulted in a serious under-estimation of the cell size. Supported by numerical simulations and by taking into account the noise in the experimental ADC as well as the uncertainty in cell size due to the segmentation procedure, we established that a two compartment STA model is adequate to explain the behavior of the experimentally obtained ADC.

Acknowledgments

This work was funded by grant ANR-13-BSV5-0014-01 (project ANImE) and by the doctoral school EOBE, University Paris Sud, XI, 91405 Orsay, France.

Animal experiments

All animal experiments were conducted in strict accordance with the recommendations and guidelines of the European Union and the French National Committee.

ORCID iDs

Jing-Rebecca Li  <https://orcid.org/0000-0001-6075-5526>

References

- Alexander D C, Hubbard P L, Hall M G, Moore E A, Ptito M, Parker G J and Dyrby T B 2010 Orientationally invariant indices of axon diameter and density from diffusion MRI *NeuroImage* **52** 1374–89
- Assaf Y, Blumenfeld-Katzir T, Yovel Y and Basser P J 2008 Axciliber: a method for measuring axon diameter distribution from diffusion MRI *Magn. Reson. Med.* **59** 1347–54
- Basser P, Mattiello J and LeBihan D 1994 MR diffusion tensor spectroscopy and imaging *Biophys. J.* **66** 259–67
- Beaulieu C and Allen P S 1994 Water diffusion in the giant axon of the squid: implications for diffusion-weighted MRI of the nervous system *Magn. Reson. Med.* **32** 579–83
- Berg H 1993 *Random Walks in Biology Princeton Paperbacks* (Princeton, NJ: Princeton University Press)
- Bihan D L, Breton E, Lallemand D, Grenier P, Cabanis E and Laval-Jeantet M 1986 MR imaging of intravoxel incoherent motions: application to diffusion and perfusion in neurologic disorders *Radiology* **161** 401–7
- Burcaw L M, Fieremans E and Novikov D S 2015 Mesoscopic structure of neuronal tracts from time-dependent diffusion *NeuroImage* **114** 18–37
- Campbell J S, Siddiqi K, Rymar V V, Sadikot A F and Pike G B 2005 Flow-based fiber tracking with diffusion tensor and q-ball data: Validation and comparison to principal diffusion direction techniques *NeuroImage* **27** 725–36
- Chabert S, Molko N, Cointepas Y, Le Roux P and Le Bihan D 2005 Diffusion tensor imaging of the human optic nerve using a non-CPMG fast spin echo sequence *J. Magn. Reson. Imaging* **22** 307–10
- Chiu D T and Zare R N 1998 Assaying for peptides in individual aplysia neurons with mass spectrometry *Proc. of the National Academy of Sciences* **95** 3338–40
- Colvin D C, Loveless M E, Does M D, Yue Z, Yankeelov T E and Gore J C 2011 Earlier detection of tumor treatment response using magnetic resonance diffusion imaging with oscillating gradients *Magn. Reson. Imaging* **29** 315–23
- Conn P and Kaczmarek L 1989 The bag cell neurons of aplysia: a model for the study of the molecular mechanisms involved in the control of prolonged animal behaviors *Molecular Neurobiology* **3** 237–73
- Dietrich O, Hubert A and Heiland S 2014 Imaging cell size and permeability in biological tissue using the diffusion-time dependence of the apparent diffusion coefficient *Phys. Med. Biol.* **59** 3081
- Does M D, Parsons E C and Gore J C 2003 Oscillating gradient measurements of water diffusion in normal and globally ischemic rat brain *Magn. Reson. Med.* **49** 206–15
- Fiala J, Spacek J and Harris K 2012 *Dendrite Structure* (Oxford: Oxford University Press) cited By 1
- Fieremans E, Jensen J H and Helpert J A 2011 White matter characterization with diffusional kurtosis imaging *NeuroImage* **58** 177–88
- Fröhlich A F, Østergaard L and Kiselev V G 2006 Effect of impermeable boundaries on diffusion-attenuated MR signal *Journal of Magnetic Resonance (San Diego, Calif. : 1997)* **179** 223–33
- Gatto R G, Ye A Q, Colon-Perez L, Mareci T H, Lysakowski A, Price S D, Brady S T, Karaman M, Morfini G and Magin R L 2019 Detection of axonal degeneration in a mouse model of huntington's disease: comparison between diffusion tensor imaging and anomalous diffusion metrics *Magn. Reson. Mater. Phys., Biol. Med.* (<https://doi.org/10.1007/s10334-019-00742-6>)
- Grant S, Buckley D, Gibbs S, Webb A and Blackband S 2001 MR microscopy of multicomponent diffusion in single neurons *Magn. Reson. Med.* **46** 1107–12
- Grebenkov D S 2007 NMR survey of reflected Brownian motion *Rev. Mod. Phys.* **79** 1077
- Hahn E L 1950 Spin echoes *Phys. Rev.* **80** 580–94
- Harkins K D, Galons J P, Secomb T W and Trouard T P 2009 Assessment of the effects of cellular tissue properties on ADC measurements by numerical simulation of water diffusion *Magn. Reson. Med.* **62** 1414–22
- Hsu E W, Aiken N R and Blackband S J 1997 A study of diffusion isotropy in single neurons by using NMR microscopy *Magn. Reson. Med.* **37** 624–7
- Ingo C, Magin R L, Colon-Perez L, Triplett W and Mareci T H 2014 On random walks and entropy in diffusion-weighted magnetic resonance imaging studies of neural tissue *Magn. Reson. Med.* **71** 617–27
- Jelescu I O 2013 Magnetic resonance microscopy of Aplysia neurons : studying neurotransmitter-modulated transport and response to stress *PhD Thesis* University Paris Sud. Thèse de doctorat dirigée par Le Bihan, Denis Physique Paris 11 2013
- Jelescu I O, Nargeot R, Bihan D L and Ciobanu L 2013 Highlighting manganese dynamics in the nervous system of aplysia californica using MEMRI at ultra-high field *NeuroImage* **76** 264–71
- Jensen J H and Helpert J A 2010 MRI quantification of non-Gaussian water diffusion by kurtosis analysis *NMR Biomed.* **23** 698–710
- Jensen J H, Helpert J A, Ramani A, Lu H and Kaczynski K 2005 Diffusional kurtosis imaging: the quantification of non-gaussian water diffusion by means of magnetic resonance imaging *Magn. Reson. Med.* **53** 1432–40
- Jespersen S N, Kroenke C D, Østergaard L, Ackerman J J and Yablonskiy D A 2007 Modeling dendrite density from magnetic resonance diffusion measurements *NeuroImage* **34** 1473–86
- Kadakkuzha B M, Akhmedov K, Capo T R, Carvalloza A C, Fallahi M and Puthanveetil S V 2013 Age-associated bidirectional modulation of gene expression in single identified r15 neuron of aplysia *BMC Genomics* **14** 880
- Kandel E R and Kupfermann I 1970 The functional organization of invertebrate ganglia *Annual Review of Physiology* **32** 193–258 PMID: 4906119.
- Khan A R, Cornea A, Leigland L A, Kohama S G, Jespersen S N and Kroenke C D 2015 3D structure tensor analysis of light microscopy data for validating diffusion MRI *NeuroImage* **111** 192–203
- Kingsley P B 2006 Introduction to diffusion tensor imaging mathematics: Part I. tensors, rotations, and eigenvectors *Concepts in Magnetic Resonance Part A* **28A** 101–22
- Kupfermann I, Carew T J and Kandel E R 1974 Local, reflex, and central commands controlling gill and siphon movements in aplysia *Journal of Neurophysiology* **37** 996–1019
- Lasek R J, Lee C K and Przybylski R J 1972 Granular extensions of the nucleoli in giant neurons of aplysia californica *J Cell Biol* **55** 237–42
- Lavdas I, Behan K C, Papadaki A, McRobbie D W and Aboagye E O 2013 A phantom for diffusion-weighted MRI (DW-MRI) *J. Magn. Reson. Imaging* **38** 173–9
- Le Bihan D, Mangin J F, Poupon C, Clark C A, Pappata S, Molko N and Chabriat H 2001 Diffusion tensor imaging: concepts and applications *J. Magn. Reson. Imaging* **13** 534–46
- Lee C H, Flint J J, Hansen B and Blackband S J 2015 Investigation of the subcellular architecture of L7 neurons of aplysia californica using magnetic resonance microscopy (MRM) at 7.8 microns *Sci. Rep.* **5** 11147
- Li J R, Calhoun D, Poupon C and Bihan D L 2013 Numerical simulation of diffusion MRI signals using an adaptive time-stepping method *Phys. Med. Biol.* **59** 441–54
- Lu L, Erokwu B, Lee G, Gulani V, Griswold M A, Dell K M and Flask C A 2012 Diffusion-prepared fast imaging with

- steady-state free precession (DP-FISP): A rapid diffusion mri technique at 7 T *Magn. Reson. Med.* **68** 868–73
- Matsumoto Y et al 2009 In vitro experimental study of the relationship between the apparent diffusion coefficient and changes in cellularity and cell morphology *Oncology Reports* **22** 641–8
- Mitra P P, Sen P N and Schwartz L M 1993 Short-time behavior of the diffusion coefficient as a geometrical probe of porous media *Phys. Rev. B* **47** 8565–74
- Mitra P P, Sen P N, Schwartz L M and Le Doussal P 1992 Diffusion propagator as a probe of the structure of porous media *Phys. Rev. Lett.* **68** 3555–8
- Mori S and Zhang J 2009 *Encyclopedia of Neuroscience* ed L R Squire (Oxford: Academic) pp 531–8
- Moussavi-Biugui A, Stieltjes B, Fritzsche K, Semmler W and Laun F B 2011 Novel spherical phantoms for q-ball imaging under *in vivo* conditions *Magn. Reson. Med.* **65** 190–4
- Musio C and Bedini C 1990 Fine structure and axonal organization in the buccal ganglia nerves of aplysia (mollusca, gastropoda) *Zoomorphology* **110** 17–26
- Ning L, Özarslan E, Westin C F and Rathi Y 2017 Precise inference and characterization of structural organization (picaso) of tissue from molecular diffusion *NeuroImage* **146** 452–73
- Palombo M, Ligneul C, Najac C, Le Douce J, Flament J, Escartin C, Hantraye P, Brouillet E, Bonvento G and Valette J 2016 New paradigm to assess brain cell morphology by diffusion-weighted MR spectroscopy *in vivo Proc. of the National Academy of Sciences* **113** 6671–6
- Palombo M, Ligneul C and Valette J 2017 Modeling diffusion of intracellular metabolites in the mouse brain up to very high diffusion-weighting: Diffusion in long fibers (almost) accounts for non-monoexponential attenuation *Magn. Reson. Med.* **77** 343–50
- Panagiotaki E, Schneider T, Siow B, Hall M G, Lythgoe M F and Alexander D C 2012 Compartment models of the diffusion MR signal in brain white matter: A taxonomy and comparison *NeuroImage* **59** 2241–54
- Pullens P, Roebroek A and Goebel R 2010 Ground truth hardware phantoms for validation of diffusion-weighted MRI applications *J. Magn. Reson. Imaging* **32** 482–8
- Radecki G, Nargeot R, Jelescu I O, Le Bihan D and Ciobanu L 2014 Functional magnetic resonance microscopy at single-cell resolution in *Aplysia californica Proc. of the National Academy of Sciences* **111** 8667–72
- Haddar H, Li J R and Schiavi S 2018 Understanding the Time-Dependent Effective Diffusion Coefficient Measured by Diffusion MRI: the IntraCellular Case *SIAM Journal on Applied Mathematics* **78** (2) 774–800
- Schoeniger J, Aiken N, Hsu E and Blackband S 1994 Relaxation-time and diffusion nmr microscopy of single neurons *J. Magn. Reson. B* **103** 261–73
- Shepherd T M, Thelwall P E, Stanisz G J and Blackband S J 2009 Aldehyde fixative solutions alter the water relaxation and diffusion properties of nervous tissue *Magn. Reson. Med.* **62** 26–34
- Sotak C H 2004 Nuclear magnetic resonance (nmr) measurement of the apparent diffusion coefficient (adc) of tissue water and its relationship to cell volume changes in pathological states *Neurochem. Int.* **45** 569–82
- Stejskal E O and Tanner J E 1965 Spin diffusion measurements: spin echoes in the presence of a time-dependent field gradient *J. Chem. Phys.* **42** 288–92
- Tanner J E and Stejskal E O 1968 restricted self-diffusion of protons in colloidal systems by the pulsed-gradient, spin-echo method *JCP* **49** 1768–77
- Torrey H C 1956 Bloch equations with diffusion terms *Phys. Rev.* **104** 563–5
- Weber T, Ziener C H, Kampf T, Herold V, Bauer W R and Jakob P M 2009 Measurement of apparent cell radii using a multiple wave vector diffusion experiment *Magn. Reson. Med.* **61** 1001–6
- Webster M, Witkin K L and Cohen-Fix O 2009 Sizing up the nucleus: nuclear shape, size and nuclear-envelope assembly *J. Cell Sci.* **122** 1477–86
- Zhang H, Hubbard P L, Parker G J and Alexander D C 2011 Axon diameter mapping in the presence of orientation dispersion with diffusion MRI *NeuroImage* **56** 1301–15
- Zhang H, Schneider T, Wheeler-Kingshott C A and Alexander D C 2012 NODDI: Practical *in vivo* neurite orientation dispersion and density imaging of the human brain *NeuroImage* **61** 1000–16
- Zhong J and Gore J C 1991 Studies of restricted diffusion in heterogeneous media containing variations in susceptibility *Magn. Reson. Med.* **19** 276–84
- Özarslan E, Basser P J, Shepherd T M, Thelwall P E, Vemuri B C and Blackband S J 2006 Observation of anomalous diffusion in excised tissue by characterizing the diffusion-time dependence of the mr signal *J. Magn. Reson.* **183** 315–23